PHOTONICS Research

On-chip path encoded photonic quantum Toffoli gate

Meng Li,[1,2,†] Chu Li,[1,2,†] Yang Chen,[3] Lan-Tian Feng,[3] Linyu Yan,[1,2] Qian Zhang,[1,2] Jueming Bao,[1,2] Bi-Heng Liu,[3] Xi-Feng Ren,[3,6] Jianwei Wang,[1,2,4,5] Shufeng Wang,[1,2,4,5] Yunan Gao,[1,2,4,5] Xiaoyong Hu,[1,2,4,5] Qihuang Gong,[1,2,4,5] and Yan Li[1,2,4,5,7]

[1]State Key Laboratory for Artificial Microstructure and Mesoscopic Physics, School of Physics, Peking University, Beijing 100871, China
[2]Frontiers Science Center for Nano-Optoelectronics, Peking University, Beijing 100871, China
[3]Key Laboratory of Quantum Information, CAS University of Science and Technology of China, Hefei 230026, China
[4]Collaborative Innovation Center of Extreme Optics, Shanxi University, Taiyuan 030006, China
[5]Peking University Yangtze Delta Institute of Optoelectronics, Nantong 226010, China
[6]e-mail: renxf@ustc.edu.cn
[7]e-mail: li@pku.edu.cn

Received 3 January 2022; revised 7 May 2022; accepted 8 May 2022; posted 9 May 2022 (Doc. ID 452539); published 9 June 2022

The quantum Toffoli gate is one of the most important three-qubit gates, but it is challenging to construct a chip according to the complicated traditional circuit. Using the optimized 3D configuration with an overpass waveguide to reduce the circuit complexity, we successfully fabricate an on-chip path encoded photonic quantum Toffoli gate enabled by the 3D capability of the femtosecond laser direct writing (FLDW) for the first time to our knowledge, whose truth-table fidelity is higher than 85.5%. Furthermore, a path encoded four-qubit controlled-controlled-controlled NOT gate is written to confirm the scalability of this resource-saving technique. This work paves the way for the FLDW of more complex and powerful photonic quantum computation chips.

https://doi.org/10.1364/PRJ.452539

1. INTRODUCTION

Nowadays, various physical systems aiming at universal quantum computation are developing toward increasing the number of controllable qubits and realizing large-scale quantum computation [1–8]. By virtue of the unique advantages of photons, such as fast traveling speed, long coherence time, simple single-qubit operation, and multiple degrees of freedom, the photonic system is considered as one of the most important and possible solutions [9]. Quantum logic gates are the building blocks of quantum circuits to construct universal quantum computers. Both destructive probabilistic two-qubit controlled-NOT (CNOT) gates [10,11] and non-destructive heralded CNOT gates [12–15] as well as three-qubit Toffoli gates [16–19] and Fredkin gates [20,21] based on bulk optical elements have been demonstrated.

Since the first photonic quantum CNOT gate on silicon-on-silica chip based on the planar lithography was reported [22], linear optical quantum computation has been developing from bulk optical elements toward integrated photonic chips for their miniaturization, stability, and scalability. More and more photonic chips are realized by the femtosecond laser direct writing (FLDW) [23–27]. On the one hand, it can fabricate waveguides with near-round cross section to support two orthogonal polarizations [28,29] for both path and polarization encoding. On the other hand, with the capability of true three-dimensional direct writing [30,31], it can optimize the design of circuit with arbitrary 3D layout to reduce the number of required elements [31] and to study the evolution of photons in two dimensions [32–34]. Based on FLDW, on-chip two-qubit path encoded CNOT gates [35] and heralded controlled phase (CZ) gates [36], polarization encoded CNOT gates [28], and heralded CNOT gates [29] have all been demonstrated, but the FLDW of multiqubit photonic quantum gates has not yet been reported.

The quantum Toffoli gate is a three-qubit logic gate that flips the logic state of the target qubit if and only if both control qubits are in logic state $|1\rangle$, which is one of the most important multiqubit gates. It enables universal reversible classical computation and is a crucial part of many quantum information processing schemes [37], such as error correction [38], fault tolerance computation [39], half adder [40], and some complex quantum algorithms like Shor's factoring and sorting algorithms [7,41] and Grover's search algorithm [42]. Up to now, the photonic quantum Toffoli gate has been realized only by bulk linear optics using different methods [16–19,43,44]. Recently, an on-chip silicon optical Toffoli gate has been proposed for reversible logic operation based on cascaded

microring resonators [45], but it is still a classical gate. It is really complex and costly to fabricate a quantum Toffoli gate based on the planar lithography or even the FLDW. Here we demonstrate the first realization, to the best of our knowledge, of an on-chip path encoded photonic quantum Toffoli gate by FLDW using the optimized 3D configuration with an overpass waveguide to reduce the circuit complexity. Furthermore, we fabricate a more complex path encoded four-qubit controlled-controlled-controlled NOT (CCCNOT) gate to confirm the scalability of this resource-saving technique and the path encoding for the quantum circuits with target qudits.

2. CIRCUIT DESIGN AND OPTIMIZATION

A. Path Encoded 3D Configuration

The quantum Toffoli gate can be decomposed by a series of single-qubit and two-qubit gates. When operating on qubits, the number of two-qubit gates is five [46] and increases to six if the two-qubit gates are restricted to CNOT or CZ gates [37]. Because photonic quantum logic gates are usually probabilistic, combining them together to realize a Toffoli gate will consume a large amount of linear optical elements and auxiliary photons based on a Knill–Laflamme–Milburn (KLM) scheme [47], which is a tough challenge to construct and characterize. Fortunately, if the target qubit is replaced by qutrit, a three-level system with logic states $|0\rangle$, $|1\rangle$, and $|2\rangle$, the quantum circuit of the post-selected Toffoli gate can be simplified efficiently [48], and only three photons are required. This scheme was first realized by polarization encoded Toffoli gate using bulk optical elements [16], combining both polarization and spatial modes to create a four-level system for target. However, it is still difficult to fabricate by FLDW and needs further optimization.

Although both path and polarization encoding can be applied for integrated quantum logic gates written by FLDW, path encoding has some advantages to realize multiqubit gates. For polarization encoded single-qubit and two-qubit gates, their circuit structures can be very simple, but the interaction lengths of their basic elements, such as waveguide waveplates [49,50] and partial polarization (dependent) directional couplers [28,29] are usually on the order of centimeters. Therefore, the total length of a polarization encoded Toffoli gate by combining several logic gates together may be too long to write, and it is unfavorable for scalability. Besides, there exist only two orthogonal polarization modes, and other degrees of freedom are required to realize a qutrit. In contrast, for path encoded quantum gates, the basic elements are directional couplers (DCs) whose interaction lengths are usually on the order of millimeters [35,51]. In addition, it is easier to scale up to high dimensional Hilbert space [52] via spatial modes and to reduce the circuit complexity by exploiting the 3D capability of FLDW.

Figure 1(a) demonstrates the optimized 3D quantum circuit of the path encoded Toffoli gate adapted from the theoretical 2D layout in Ref. [48]. In this 3D circuit, there are two control qubits C_1, C_2 and one target qutrit T that has three paths marked 2, 3, and 4. Path 2 and path 3 correspond to logic states $|1\rangle$ and $|0\rangle$ of target qutrit T, respectively, while path 4 corresponding to the additional logic state $|2\rangle$ is a vacuum mode. It should be noted that the beam splitter in Ref. [48] is assumed

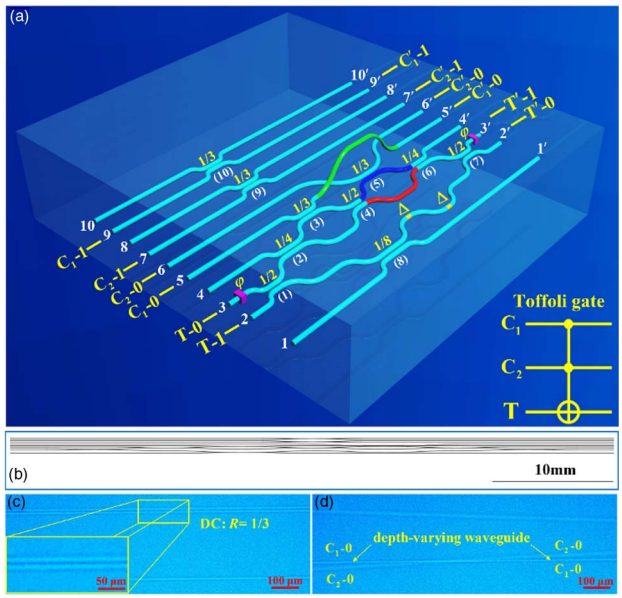

Fig. 1. Circuit design of the Toffoli gate. (a) Schematic of the 3D layout of the path encoded three-qubit Toffoli gate for FLDW. The 3D quantum circuit is adapted from the 2D theoretical work in Ref. [48], where the blue, red, and green curves correspond to the top-path, bottom-path, and depth-varying overpass waveguides, respectively. There are 10 DCs in this circuit, and the number marked on each DC stands for reflectivity R. DCs (2), (3), and (4) construct a local classical interferometer. Two parts (yellow curves) marked Δ stand for path compensation for the global unsymmetrical MZ interferometer. The depth change of the overpass waveguide is 20 μm. Two magenta boxes marked φ represent additional phase shifts ($-\pi/2$) that should be compensated at the input and output ports. (b) The CAD layout of the Toffoli gate. (c) Micrograph of the DC with the reflectivity of 1/3 and the enlarged view of the coupling region. (d) Micrograph of the waveguides in different depths without crossing.

to be asymmetric in phase, where a phase flip is induced by reflection off one surface indicated by a dotted line, but all other components experience no phase change, while the directional coupler here is symmetric, which means that all DCs add a $\pi/2$ phase to each wave that is evanescently coupled (transmitted). The transformation matrix of a DC is shown in Eq. (1), where R is the reflectivity:

$$M_{\mathrm{DC}} = \begin{pmatrix} \sqrt{R} & i\sqrt{1-R} \\ i\sqrt{1-R} & \sqrt{R} \end{pmatrix}. \tag{1}$$

The original circuit in Ref. [48] is actually a controlled-controlled Z (CCZ) gate, which still needs two single-qubit Hadamard (H) gate operations on the target qubit to transform into a Toffoli gate. However, the two added H gates construct a global unsymmetrical Mach–Zehnder (MZ) interferometer connected by path T-0 to T′-1 and path T-1 to T′-0, which results in four crossings among waveguides and makes the photonic circuit more complex. To construct an efficient quantum circuit with succinct structures, we rearrange the layout to reduce the circuit complexity by changing the position of DC (5) from the bottom path (red curve) to the top path (blue curve) to avoid crossing of waveguides and by modifying the reflectivity of DC (2) from 3/4 to 1/4 to match the new circuit.

Furthermore, we introduce a depth-varying 3D overpass waveguide for path 5 indicated as a green curve to eliminate the last remaining crossing, which can only be realized by FLDW technique. It is the key factor to avoid crossing and coupling with the waveguide for path 6, which reduces the number of required elements and demonstrates the advantage of FLDW to optimize the quantum circuit using 3D architectures. To guarantee the equality of optical path between two arms of the global unsymmetrical MZ interferometer, two parts for path compensation Δ (yellow curves) are added into the bottom arm. Considering that the two H gates [DCs (1) and (7)] are not actually standard Hadamard gates, two additional phase shifts φ (magenta boxes) should be added to the input and output ports of the target qutrit, for instance, $-\pi/2$ at T-0 and $-\pi/2$ at T′-1, to make the circuit in Fig. 1(a) a true quantum Toffoli gate, which can be compensated by outside delay lines.

After efficient optimization using 3D configuration, the photonic circuit has 10 DCs, including four kinds of reflectivity 1/2, 1/3, 1/4, and 1/8, which can be precisely and repeatedly fabricated by FLDW. For each DC, the bending radius is set as 60 mm to make additional bending loss lower than 0.50 dB/cm, and the interaction distance is fixed to 8 μm to acquire enough coupling strength without geometric overlap. With fixed interaction distance, the interaction lengths are determined by the method in our previous works [35,51]. The interaction lengths of DCs with reflectivity 1/2, 1/3, 1/4, and 1/8 are $L_{1/2} = 0.470$ mm, $L_{1/3} = 0.692$ mm, $L_{1/4} = 0.811$ mm, and $L_{1/8} = 1.023$ mm, respectively. For the global unsymmetrical MZ interferometer, the bending segments of the two arms are fabricated identically, and the difference is at the straight waveguides, so the optical path compensation $\Delta = 0.416$ mm by Eq. (2):

$$\Delta = \frac{2L_{1/3} + L_{1/2} - L_{1/8}}{2}. \tag{2}$$

The depth-varying 3D overpass waveguide structure with a bending radius of 120 mm and a depth change of 20 μm can minimize the depth-varying bending loss and avoid undesired coupling with other waveguides. The size of the Toffoli gate is 50 mm × 1.27 mm. Thus, it can be seen that the photonic circuit with 3D configuration is well optimized, but its complexity still greatly exceeds those of the existing quantum gates written by FLDW. The CAD layout and the micrographs of the Toffoli gate are presented in Fig. 1(b) and Figs. 1(c) and 1(d), respectively. The fabrication parameters for the Toffoli gate can be found in Appendix A, and the experimental characterization results of a typical Toffoli gate with classical light are shown in Appendix B.

B. Function of the Classical and Quantum Interferences

The theoretical success probability of this probabilistic post-selected Toffoli gate based on Ref. [48] is 1/72, which is higher than that of most other schemes and needs fewer photons [53,54]. Similar to the path encoded two-qubit CNOT gate we realized before [35], the successful performance of this Toffoli gate also depends on the combination of two kinds of interferences: one is the classical MZ interference, and the other is the quantum Hong–Ou–Mandel (HOM) interference [55]. As shown in Fig. 1, there are two classical interferences in this circuit, where one happens in the global classical MZ interferometer, and the other occurs in the local classical interferometer constructed by DCs (2), (3), and (4). The performance of the classical interferences relies on the accurate reflectivity of DCs and completely symmetrical optical paths for two arms, meaning that all phase differences within classical interferometers should be zero. There also exist two quantum interferences, where the one at the DC (3) is the first quantum interference, and the other at the DC (5) is the second one. When one photon from C and the other photon from T are mixed in the DC with the reflectivity of 1/3 simultaneously, they will undergo a partial bunching effect and get a π phase shift due to the quantum interference of indistinguishable photons, which can change the output states of the classical interferometers to guarantee the correct logic operation. In principle, for this adapted circuit, when the first quantum interference happens, the second quantum interference will not happen, that is to say, the two quantum interferences will not occur successively. The function of the first quantum interference is to switch the coupling path of one of the coincidence photons that outputs from the local classical interferometer from the top (blue curve) to the bottom (red curve), resulting in the final flip of the target logic state indirectly. The function of the second quantum interference is to directly realize the final flip of the target logic state due to the π phase shift when the first quantum interference does not happen. For the polarization encoded quantum Toffoli gate using bulk optical elements, it requires the quantum interferences to happen 0, 1, or 2 times for all input states [16], where the dependent photon pair from the first spontaneous parametric down conversion (SPDC) source interferes non-classically at the first partially polarizing beam splitter (PPBS1), and then one photon goes on to interfere non-classically with a third photon, independently generated from the second SPDC source, at PPBS2. The manipulation of two successive non-classical interferences requiring perfect quantum interference between both dependent and independent photons is challenging, and the contrast drops dramatically. In contrast, for this optimized path encoded quantum Toffoli gate, it only requires the quantum interference to happen 0 or 1 time, which means that the photons in the first quantum interference will not interfere with the photons in the second quantum interference, which can greatly reduce the difficulty in characterization to achieve a relatively higher fidelity. Meanwhile, this optimized and simplified circuit configuration is much simpler than that with two sequential quantum interferences and makes it easier to fabricate. The performance of the quantum interference can be evaluated by measuring the two-photon quantum interference visibility (V), which depends not only on the performance of the chip but also on the quality of the quantum source.

3. EXPERIMENTAL RESULTS

A. Quantum Interference Visibilities

The optimized quantum Toffoli gate requires four-fold coincidence to characterize using the quantum source generated by the SPDC process. Three photons are required for performing the logic operation of this probabilistic post-selected Toffoli

gate, and the fourth photon is for the trigger. The post selection via the three-fold coincidence measurement is used to guarantee the correct outputs of three-photon combinations and to filter out all unwanted combinations. The correct logic operation mainly depends on two-photon quantum interferences. The quantum interference visibilities at the two DCs with reflectivity 1/3 [DCs (3) and (5)] are characterized using a high-quality type-I SPDC time-correlation two-photon source whose brightness is about 8 kHz, and the interference visibility can reach 98% on a balanced (1:1) fiber beam splitter (FBS) [35,51]. When the input two-photon combinations are (5, 2), (5, 3), (6, 2), and (6, 3), the quantum interference curves of the post-selected output two-photon combinations (5′, 2′), (5′, 3′), (6′, 2′), and (6′, 3′) are shown in Figs. 2(a), 2(b), 2(c), and 2(d), respectively. Without subtracting the accidental coincidence counts, the raw interference visibilities are 86.5% ± 2.8%, 89.5% ± 2.5%, 98.8% ± 0.9%, and 98.3% ± 0.9%, respectively. The uncertainty obeys the rule of Poisson statistics.

The insets demonstrate the main evolution of two coincident photons in the chip, which is determined by the combination of classical and quantum interferences. For example, when the input two-photon combination is (5, 2) and the relative delay between two indistinguishable photons mixed at the DC (3) is 0 as shown in Fig. 2(a), the coincidence counts of post-selected output two-photons from (5′, 2′) disappear (hollow circles), resulting in the dip of the quantum interference curve, while that of the combination (5′, 3′) basically remains unchanged (filled circles). The other three situations in Figs. 2(b)–2(d) are similar. The high interference visibility of the second quantum interference demonstrates the high quality of the waveguide modes and the fabrication precision. The visibility of the first quantum interference is a little lower, which may be due to the incomplete transformation of output photons from the top path (blue curve) to the bottom path (red curve) for the imperfect classical interference in the local classical interferometer. In addition, the imperfection of the polarization control of input photons can also result in a reduced interference visibility, when the half-wave plates and polarization controllers do not well compensate the rotation of polarization states in different optical fibers. In Fig. 2(c), the coincidence counts at the right of the non-interference zone being lower than that at the left are due to the slight misalignment of the delay line translation and the propagation direction of the generated photons. The experimental results are consistent with the theoretical expectation, suggesting the high quality of the key parts of the Toffoli gate chip.

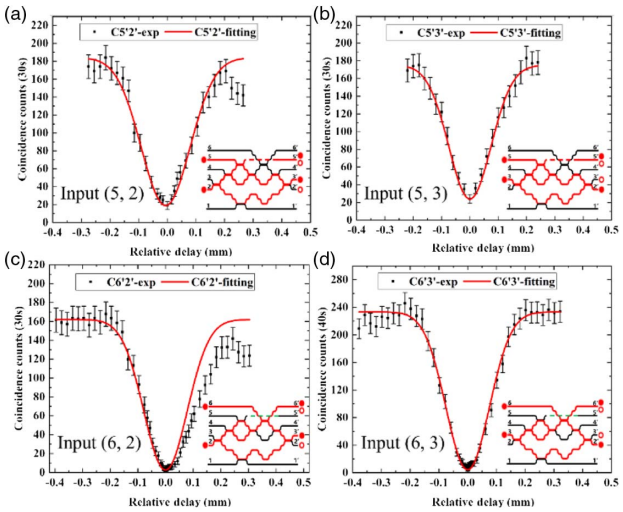

Fig. 2. Two-photon quantum interference curves. Coincidence counts of post-selected output two-photon combinations (i', j') denoted as $Ci'j'$ for different input two-photon combinations (i, j) denoted as Input (i, j) as a function of the relative delay of photons' input in the i and j ports: (a) input (5, 2); (b) input (5, 3); (c) input (6, 2); (d) input (6, 3). From the interference curves with a deep dip, the HOM interference visibilities are (a) 86.5% ± 2.8%, (b) 89.5% ± 2.5%, (c) 98.8% ± 0.9%, and (d) 98.3% ± 0.9%, respectively. The error bars are all calculated by assuming Poisson statistics. The insets demonstrate the main evolution of two photons in the chip. The pairs of filled circles are coincident photons, and the pairs of the hollow circles represent the disappearance of coincident photons due to the quantum interferences.

B. Reconstructed Truth Table of the Toffoli Gate

The quantum four-photon characterization system for the Toffoli gate is shown in Fig. 3(a) (details can be seen in

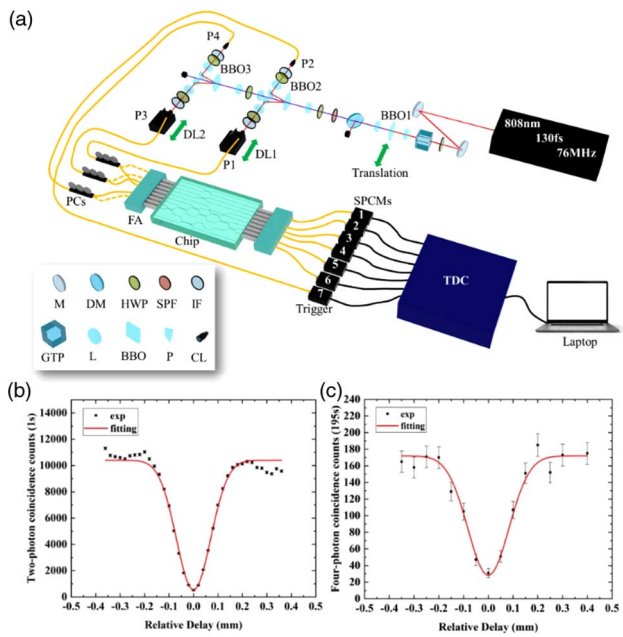

Fig. 3. Schematic of the quantum characterization system. (a) The 808 nm femtosecond laser pulses pass through a frequency-doubling crystal (BBO1) to generate linearly polarized 404 nm ultraviolet pulses, and the ultraviolet pulses are focused on two cascaded beamlike II BBO crystals (BBO2&BBO3) to produce two pairs of photons with quantum correlation. The photons are injected into chips and collected to make four-fold coincidence measurement. M, mirror; DM, dichroic mirror; HWP, half-wave plate; SPF, short-pass filter (<650 nm); IF, interference filters at 808 nm; GTP, Glan–Taylor polarizer; L, lens; BBO, β–BaB_2O_4 crystal; P, prism; CL, coupling lens; SPCMs, single-photon counting modules; FA, fiber array; DL, delay line; TDC, time-to-digital converter. (b) Two-photon quantum interference curve of the dependent photons 1&2 on a balanced FBS ($V = 94.7\% \pm 0.2\%$). (c) Four-photon quantum interference curve of the independent photons 2&3 on a balanced FBS ($V = 83.1\% \pm 3.2\%$). The error bars are all calculated by assuming Poisson statistics.

Appendix D). As shown in Figs. 3(b) and 3(c), the two-photon interference visibility of the dependent photon pair 1&2 on a balanced FBS is about 94.7% ± 0.2%, while the four-photon interference visibility is about 83.1% ± 3.2% when the interaction photon pair 2&3 on the balanced FBS is independent, which demonstrates a significant difference in the indistinguishability between dependent and independent photons. To reconstruct the truth table as accurately as possible, we need to swap the control photons to achieve a higher quantum interference visibility by utilizing photon pair 1&2 to conduct each quantum interference.

According to post-selected four-fold coincidence counts, the truth table of the fabricated Toffoli gate at the computation basis is reconstructed after a long-time data collection. The longest time to complete the four-fold coincidence measurement is up to 5 days when the two control qubits are in state $|00\rangle$. We define the contrast $C = P_{\text{ideal}}/(P_{\text{ideal}} + P_{\text{flip}})$, where P_{ideal} is the probability to obtain the ideal output state and P_{flip} is the probability to obtain the flipped output state due to quantum interference when the relative delay is zero. For inputs $|C_1C_2T\rangle = |110\rangle$ and $|111\rangle$, no quantum interference is required for the correct logic operation, and the contrasts of outputs are 0.911 ± 0.001 and 0.930 ± 0.001. Inputs $|C_1C_2T\rangle = |010\rangle$ and $|011\rangle$ require the quantum interference between photons C_1 and T (the first quantum interference), and the contrasts of outputs are 0.821 ± 0.014 and 0.854 ± 0.011, while inputs $|C_1C_2T\rangle = |100\rangle$ and $|101\rangle$ require quantum interference between photons C_2 and T (the second quantum interference), and the contrasts of outputs are 0.860 ± 0.010 and 0.865 ± 0.012. For inputs $|C_1C_2T\rangle = |000\rangle$ and $|001\rangle$, all three photons are input to the main body of the DC network, but when quantum interference between photons C_1 and T happens, the coincidence photons of C_1 and T will not interact with photons C_2, and the contrasts of outputs are 0.841 ± 0.016 and 0.755 ± 0.031. It should be noted that we exchange the photons 1 and 3 originally for control qubit C_1 and C_2 when inputs are $|C_1C_2T\rangle = |100\rangle$ and $|101\rangle$ to acquire a better effect of quantum interference.

The basic quantum characterization is the truth table, which reflects the classical action of a quantum logic gate. The reconstructed truth table depicted in Fig. 4 shows the population of all computation basis output states after applying the Toffoli gate operation to each of the computation basis input states. The overlap between two truth tables, the experimental U_{exp} with respect to the ideal one U_{ideal}, namely truth-table fidelity $F = \text{Tr}(U_{\text{ideal}}^{+} U_{\text{exp}})/8 = 85.5\% \pm 0.6\%$, is higher than that (81% ± 3%) of polarization encoded Toffoli gate using bulk optical elements [16] based on the same principle in Ref. [48]. Furthermore, considering the two-photon experimental results in Fig. 2, the measured truth-table fidelity can be further improved by more precise polarization control of input photons and better photon source. To reduce the measurement time, we increase the pump power to improve the brightness of the quantum four-photon source to 20 Hz, but this results in the deterioration of the fidelity due to the increase of photon distinguishability and the unwanted high-order multiphoton noise. For example, the two-photon interference visibility of the type-I source can reach 98%, but that of the dependent photons 1&2 in a beamlike II source is about 95% at maximum and maintains at 92% during the long-time measurement, and four-photon interference visibility of the independent photons 2&3 is just 83%. Assuming the coincidence counts of ideal and flipped output states are c_i and c_f, respectively, and the interference visibility of quantum source on a balanced FBS is V, when the relative delay is at non-interference zone, $c_f \approx 2c_i$, and when the relative delay is zero, $c_f \approx 2c_i \cdot (1 - V)$, the upper bound of the contrast is $C = c_i/[c_i + 2c_i(1 - V)] = 1/(3 - 2V)$. Thus the contrast of output photons for inputs $|C_2T\rangle = |00\rangle$ and $|01\rangle$ using two-photon source can exceed 95% when $V = 0.98$, but that using four-photon source is only about 86% when $V = 0.92$. If a better high-quality quantum four-photon source with brightness of 20 Hz like that in Ref. [56] is adopted, the interference visibilities of dependent and independent photons can reach 98% and 97%, respectively, and thus the measured average fidelity of the truth table of this Toffoli gate is expected to be improved to higher than 90%.

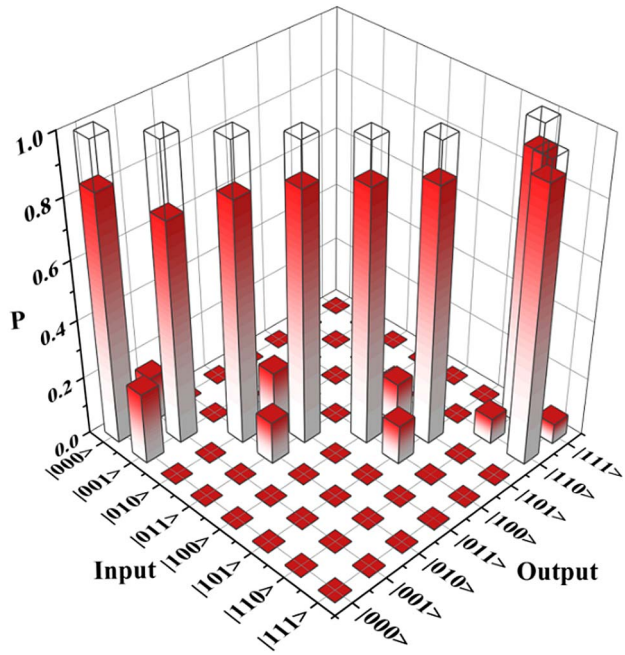

Fig. 4. Truth table of the path encoded three-qubit Toffoli gate at computation basis. The filled bars are the normalized experimental reconstructed data, and the unfilled ones are the ideal values. The average fidelity of the truth table of this Toffoli gate is 85.5% ± 0.6%.

In addition to the truth table, the complete quantum characterization of a quantum gate still requires the quantum state tomography and quantum process tomography by using maximum likelihood estimation to reconstruct physical states and by using Monte Carlo method with Poissonian statistics for error analysis. To conduct the full quantum characterization of this quantum Toffoli gate, it is required to input path encoded superposition states and to perform multiple projective measurements. However, this Toffoli gate is a passive chip without tunable phase shifters, and the off-chip superposition state preparation and the input/output between the free space

and the chip are challenging and time-consuming. Up to now, we have just characterized the truth table. To give more details about the performance of the quantum Toffoli gate for multiple inputs, the loss analysis is carried out in Appendix C.

4. SCALING UP TO FOUR-QUBIT CCCNOT GATE

Furthermore, if the target is a ququart, a four-level system with logic states $|0\rangle$, $|1\rangle$, $|2\rangle$, and $|3\rangle$, the quantum circuit can be scalable to four-qubit CCCNOT gate. Quantum CCCNOT gate is a four-qubit quantum logic gate that flips the logic state of the target qubit if and only if all three control qubits are in logic state $|1\rangle$. As shown in Fig. 5(a), we design an efficient CCCNOT gate consisting of one CCZ gate, one CZ gate, and two H gates. There are 15 DCs in total with five kinds of reflectivity: 1/2, 1/3, 1/4, 1/9, and 1/18. There are two depth-varying overpass waveguides marked by green and light green curves, which can remove all undesired crossings skillfully and avoid coupling among several waveguides, further demonstrating the advantage of 3D configuration. However, it is quite complex to realize such a circuit using planar lithography to arrange plenty of crossings in the layout. Similarly, there are also two parts marked Δ used for path compensation for the global unsymmetrical MZ interferometer. However, to guarantee the correction of logic operation, one segment is added to generate a phase shift $\Delta\phi = \pi$ by deforming the waveguides marked by the red curve. Two additional phase shifts φ (magenta boxes) are also added to the input and output ports of the target qutrit, for instance $-\pi/2$ at T-0 and $-\pi/2$ at T′-0, to make the circuit in Fig. 5(a) a true quantum CCCNOT gate.

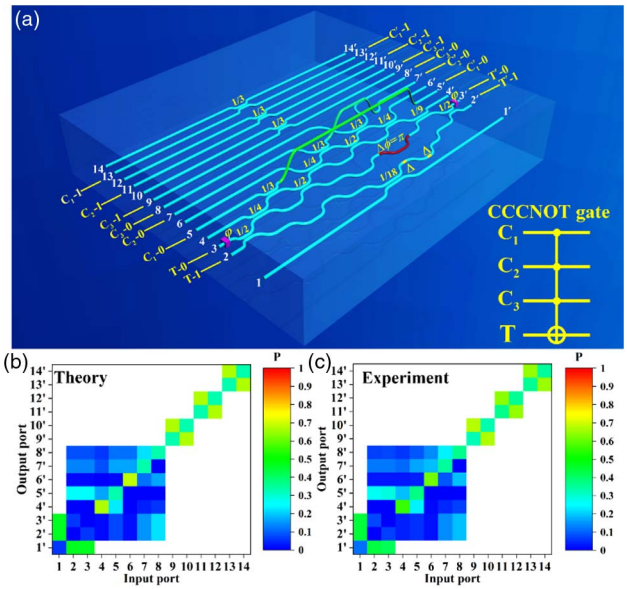

Fig. 5. Schematic of the 3D layout of the path encoded four-qubit CCCNOT gate for FLDW and the experimental characterization with classical light. (a) The green and light green curves correspond to depth-varying overpass waveguides, and the red curve stands for the waveguides deformed to generate a phase shift $\Delta\phi = \pi$. Two parts marked Δ correspond to path compensation for the global MZ interferometer, and two magenta boxes marked φ represent additional phase shifts $(-\pi/2)$ that should be compensated at the input and output ports. (b) Theoretical output power distribution for each single port input. (c) Experimental output power distribution for each single port input when the injected laser is centered at 808 nm with V polarization. The similarity (S) of the output power distribution for this CCCNOT gate is 99.2% ± 0.8%.

Based on FLDW technique, we have fabricated the path encoded CCCNOT gate chip. The size of the chip is 70 mm × 1.905 mm. The interaction lengths of DCs with reflectivity 1/2, 1/3, 1/4, 1/9, and 1/18 are 0.350, 0.600, 0.735, 1.005, and 1.155 mm, respectively. Therefore, the optical path compensation $\Delta = 0.198$ mm, which is determined by Eq. (3):

$$\Delta = \frac{2L_{1/3} + L_{1/2} - L_{1/18}}{2}. \tag{3}$$

The success probability of this probabilistic post-selected CCCNOT gate is 1/486, which is much lower than that of the Toffoli gate. The theoretical truth table of an ideal CCCNOT gate is a 16 × 16 matrix where elements corresponding to $(|ijkl\rangle, |ijkl\rangle)_{i\times j\times k=0}$, $(|1110\rangle, |1111\rangle)$, and $(|1111\rangle, |1110\rangle)$ are 1, and the others are 0. To completely conduct the quantum characterization of this chip, it needs four indistinguishable photons and will take much more time. Thus, we only conduct the experimental characterization with classical light, whose experimental results match quite well with the theory as shown in Figs. 5(b) and 5(c). The measured similarity is $S = [\sum_i (\sum_j \sqrt{p_{ij} q_{ij}})^2]/14 = 99.2\% \pm 0.8\%$, where i (j) is the input (output) port number and p_{ij} (p_{ij}) is the theoretical (experimental) value of power distribution. This demonstrates the potential in the fabrication of the path encoded four-qubit CCCNOT gate using FLDW and the scalability for multiqubit photonic quantum gates using this resource-saving technique.

5. CONCLUSION

We demonstrate the first successful FLDW of an on-chip path encoded three-qubit photonic quantum Toffoli gate using the optimized 3D configuration with an overpass waveguide to reduce the circuit complexity, to the best of our knowledge. The measured average fidelity of the truth table is 85.5% ± 0.6%, which is higher than that of the polarization encoded quantum Toffoli gate using bulk optical elements (81% ± 3%) based on the same principle. Furthermore, we also demonstrate the potential in the fabrication of the path encoded four-qubit CCCNOT gate with two overpass waveguides and the scalability for this resource-saving technique and the path encoding for multiqubit gates. The unique 3D architectures with optimized layout and the 3D capability of FLDW make it feasible to fabricate multiqubit gate chips. By exploration of the hybrid scheme of utilizing multi-degrees of freedom of photons [19,44,57,58], such as the path, polarization, and orbital angular momentum (OAM) in a chip, it is expected to further simplify the circuit structures, reduce the photon resource requirements, and even increase the success probability. The successful fabrications of multiqubit photonic quantum logic gates pave the way for the FLDW of more complex and powerful photonic quantum computation chips, such as chips to perform fault tolerance quantum computation and quantum factoring, sorting, and search algorithms.

APPENDIX A: FABRICATION OF QUANTUM GATES

The quantum gate chips consist of waveguides fabricated in borosilicate glass (Eagle 2000, Corning) by femtosecond laser pulses centered at 1030 nm with a duration of 240 fs, which are focused 170 μm beneath the surface of the glass by a microscope objective with a numerical aperture NA = 0.5 (RMS20X-PF, Olympus). The sample is translated at a constant speed using a computer-controlled high-precision three-axis air-bearing stage (FG1000-150-5-25-LN, Aerotech).

For the fabrication of Toffoli gates, the pulse energy is 386 nJ at a repetition rate of 1 MHz, and the translation speed is 20 mm/s. For the fabrication of CCCNOT gates, the pulse energy is 420 nJ at a repetition rate of 1 MHz, and the translation speed is 25 mm/s.

For the curved segments of DCs, the bending radius is set as 60 mm; but for the depth-varying 3D overpass waveguide structure, it is connected by two consecutive reverse arc waveguides with a bending radius of 120 mm and a depth change of 20 μm to minimize the bending loss and to avoid undesired coupling with other waveguides.

APPENDIX B: EXPERIMENTAL CHARACTERIZATION OF THE TOFFOLI GATE WITH CLASSICAL LIGHT

By injecting 808 nm CW laser with V polarization into one input port i of the Toffoli gate chip in turn, we measure the power distribution P of the output port j to complete the characterization in the classical regime. The theoretical and experimental values of the characterization of the Toffoli gate with classical light are shown in Figs. 6(a) and 6(b). According to the similarity $S = [\sum_i (\sum_j \sqrt{p_{ij} q_{ij}})^2]/10 = 98.2\% \pm 1.7\%$, where i (j) is the input (output) port number and p_{ij} (q_{ij}) is the theoretical (experimental) value of the power distribution, the deviation between the experimental data and theoretical value is very small. Thus, the depth-varying overpass waveguide structure with optimized fabrication parameters has a relative low loss and can prevent the crossing and coupling with other waveguides, so it has a small impact on the output power distribution.

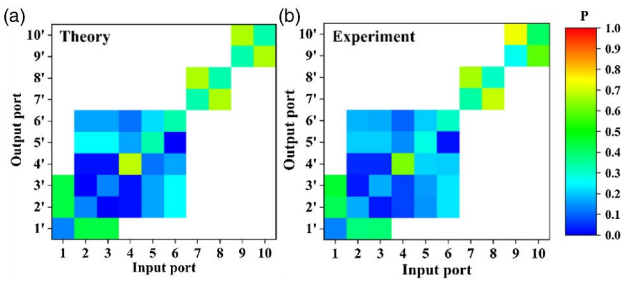

Fig. 6. Experimental characterization of a typical Toffoli gate with classical light. (a) Theoretical output power distribution for each input port. (b) Experimental output power distribution for each single input port when the injected laser is centered at 808 nm with V polarization. The similarity (S) of the output power distribution for this Toffoli gate is 98.2% ± 1.7%.

APPENDIX C: LOSS ANALYSIS AND PRE-COMPENSATON

To carry out the loss analysis, we use 808 nm CW laser with V polarization to measure the losses for waveguides in the Toffoli gate chip. Table 1 demonstrates the normalized output power distribution and the loss analysis for each single input. The transmissivity is the ratio of the total power of all output ports and the same input power for each single input, and the corresponding measured insertion loss is IL-exp = $-10 \times \lg(\text{Transmissivity})$. The propagation loss (PL) of the straight waveguide is about 0.39 dB/cm, and the additional bending loss (BL) for the curved waveguide with a 60 mm radius is about 0.49 dB/cm, while the depth-varying bending loss (DVL) for the overpass waveguide with a 120 mm radius is about 2.02 dB/cm (the total loss is about 1.25 dB). The coupling loss (CL) due to the mode mismatch is about 0.75 dB, and the Fresnel reflection loss (FL) is about 0.18 dB/facet. For each single input, the theoretical insertion loss (IL) can be calculated by summing all losses together according to the paths the input photons walk through by Eq. (C1):

$$\text{IL} = \text{CL} + 2\text{FL} + \sum_m \alpha_m \text{PL} \cdot L_m^s + \sum_n \beta_n (\text{PL} + \text{BL}) \cdot L_n^c + \sum_k \gamma_k (\text{PL} + \text{DVL}) \cdot L_k^d. \quad \textbf{(C1)}$$

The different lengths of the straight waveguides, the curved waveguides with a 60 mm radius, and the depth-varying waveguides with a 120 mm radius are represented by L_m^s, L_n^c, and L_k^d. The power ratio coefficients α_m, β_n, and γ_k are related to the combination of reflectivity of DCs. As for the loss analysis, though there exists experimental measurement error, the theoretical prediction of the insertion loss for each single input is basically consistent with the experimental results as shown in Table 1. To guarantee the equal probability of post-selected output-photon combination, DCs (9) and (10) are used to balance the amplitude. However, the real insertion losses between the input of control qubit C_1–0 (C_2–0) and C_1–1 (C_2–1) are different, which means that the output amplitude depends on the input state and the particular path through the interferometers the signals take, so pre-compensation is required on the inputs for superposition states. For example, the input superposition state for C_1 should be compensated as $|\psi_{\text{comp}}\rangle_{C_1} = a_0|0\rangle + \sqrt{0.37/0.45}a_1|1\rangle$, and that for C_2 should be $|\psi_{\text{comp}}\rangle_{C_2} = a_0|0\rangle + \sqrt{0.41/0.47}a_1|1\rangle$. In contrast, the insertion losses for T-0 and T-1 are almost equal, so no compensation is required.

APPENDIX D: QUANTUM CHARACTERIZATION USING FOUR-PHOTON SOURCE

A 76 MHz Ti:sapphire oscillator (Mira 900F) produces 130 fs pulses at 808 nm (1.4 W average power), which are upconverted to 404 nm light in a 2-mm-thick beta-barium borate (BBO) crystal cut for type-I second-harmonic generation. The 404 nm light is focused by an objective with a focal length of 150 mm to pump two cascaded 2-mm-thick AR-coated BBO crystals phase-matched for beamlike II SPDC to generate

Table 1. Normalized Output Power Distribution and Loss Analysis for Each Single Input

	Normalized Distribution												
i	$j = 10'$	$9'$	$8'$	$7'$	$6'$	$5'$	$4'$	$3'$	$2'$	$1'$	Transmissivity	IL-exp (dB)	IL-theory (dB)
10	0.41	0.59									0.46	3.42	3.43
9	0.74	0.26									0.45	3.52	3.43
8			0.31	0.69							0.47	3.24	3.43
7			0.65	0.35							0.47	3.31	3.43
6					0.33	0.01	0.20	0.23	0.23		0.41	3.92	3.92
5					0.19	0.29	0.20	0.16	0.16		0.37	4.34	4.46
4					0.10	0.14	0.62	0.07	0.07		0.46	3.37	4.32
3					0.18	0.20	0.04	0.16	0.03	0.38	0.31	5.15	4.53
2					0.19	0.20	0.04	0.03	0.16	0.38	0.31	5.09	4.53
1								0.45	0.42	0.13	0.35	4.50	4.38

two groups of 808 nm two-photon pairs with quantum correlation. The photons output from ports 1, 2, and 3 are spectrally filtered by 808 nm interference filters (IFs) with 3 nm bandwidth to guarantee the indistinguishability of spectra, while the bandwidth of IF for photons output from port 4 is 10 nm to improve the trigger efficiency by increasing the single-channel counts. The coincidence rate of the first two-photon pair (1&2) is about 40 kHz, and that of the second (3&4) is about 30 kHz. Therefore, we achieve a four-photon coincidence rate of 15–20 Hz. The two-photon interference visibility of dependent photons (1&2) is 0.947, and the four-photon interference visibility of independent photons (2&3) is 0.831.

Three of the photons (1, 2, 3) are coupled into single-mode fibers and injected into the chip using a butt-coupled eight-channel V-grove fiber array. A six-axis precise alignment stage provides all the degrees of freedom necessary to achieve optimal simultaneous coupling into all eight input modes. The same setup is used at the output to realize the optimal coupling from the chip to the output V-grove fiber array, and then the output photons are transmitted to the single-photon counting modules (SPCMs) 1–6, while photons output from port 4 are directly detected by the fiber-coupled single- photon detector 7 for the trigger signal. Due to the length difference of fibers between the trigger photon and other photons, the time delay for the trigger is set as 30 ns. A programable high-speed multichannel time-to-digital converter (Time Tagger Ultra, Swabian instruments) is used to handle all the signals from the SPCMs to conduct four-fold coincidence measurements. Half-wave plates and polarization controllers (PCs) are used to ensure that photons input to chip are in V polarization and guarantee the indistinguishability of polarization mode. Delay lines 1 and 2 are used to adjust the arrival time of photons at 1/3 DCs to maintain the temporal indistinguishability.

Funding. National Key Research and Development Program of China (2018YFB1107205, 2016YFA0301302); National Natural Science Foundation of China (12134001, 61590933, 61590932, 11527901, 11774333, 62061160487); Joint Fund for Equipment Pre-research Space Science and Technology (6141B06140601); Strategic Priority Research Program of the Chinese Academy of Sciences (CAS) (XDB24030601); Fundamental Research Funds for the Central Universities.

Disclosures. The authors declare no conflicts of interest.

Data Availability. Data underlying the results presented in this paper are not publicly available at this time but may be obtained from the authors upon reasonable request.

†These authors contributed equally to this paper.

REFERENCES

1. Y. Wu, W.-S. Bao, S. Cao, F. Chen, M.-C. Chen, X. Chen, T.-H. Chung, H. Deng, Y. Du, D. Fan, M. Gong, C. Guo, S. Guo, L. Han, L. Hong, H.-L. Huang, Y.-H. Huo, L. Li, N. Li, S. Li, Y. Li, F. Liang, C. Lin, J. Lin, H. Qian, D. Qiao, H. Rong, H. Su, L. Sun, L. Wang, S. Wang, D. Wu, Y. Xu, K. Yan, W. Yang, Y. Yang, Y. Ye, J. Yin, C. Ying, J. Yu, C. Zha, C. Zhang, H. Zhang, K. Zhang, Y. Zhang, H. Zhao, Y. Zhao, L. Zhou, Q. Zhu, C.-Y. Lu, C.-Z. Peng, X. Zhu, and J.-W. Pan, "Strong quantum computational advantage using a superconducting quantum processor," Phys. Rev. Lett. **127**, 180501 (2021).
2. F. Arute, K. Arya, R. Babbush, D. Bacon, J. C. Bardin, R. Barends, R. Biswas, S. Boixo, F. G. S. L. Brandao, D. A. Buell, B. Burkett, Y. Chen, Z. Chen, B. Chiaro, R. Collins, W. Courtney, A. Dunsworth, E. Farhi, B. Foxen, A. Fowler, C. Gidney, M. Giustina, R. Graff, K. Guerin, S. Habegger, M. P. Harrigan, M. J. Hartmann, A. Ho, M. Hoffmann, T. Huang, T. S. Humble, S. V. Isakov, E. Jeffrey, Z. Jiang, D. Kafri, K. Kechedzhi, J. Kelly, P. V. Klimov, S. Knysh, A. Korotkov, F. Kostritsa, D. Landhuis, M. Lindmark, E. Lucero, D. Lyakh, S. Mandrà, J. R. McClean, M. McEwen, A. Megrant, X. Mi, K. Michielsen, M. Mohseni, J. Mutus, O. Naaman, M. Neeley, C. Neill, M. Y. Niu, E. Ostby, A. Petukhov, J. C. Platt, C. Quintana, E. G. Rieffel, P. Roushan, N. C. Rubin, D. Sank, K. J. Satzinger, V. Smelyanskiya, K. J. Sung, M. D. Trevithick, A. Vainsencher, B. Villalonga, T. White, Z. J. Yao, P. Yeh, A. Zalcman, H. Neven, and J. M. Martinis, "Quantum supremacy using a programmable superconducting processor," Nature **574**, 505–510 (2019).
3. J. Wang, F. Sciarrino, A. Laing, and M. G. Thompson, "Integrated photonic quantum technologies," Nat. Photonics **14**, 273–284 (2020).
4. X.-L. Wang, Y.-H. Luo, H.-L. Huang, M.-C. Chen, Z.-E. Su, C. Liu, C. Chen, W. Li, Y.-Q. Fang, X. Jiang, J. Zhang, L. Li, N.-L. Liu, C.-Y. Lu, and J.-W. Pan, "18-qubit entanglement with six photons' three degrees of freedom," Phys. Rev. Lett. **120**, 260502 (2018).
5. A. Bermudez, X. Xu, R. Nigmatullin, J. O'Gorman, V. Negnevitsky, P. Schindler, T. Monz, U. G. Poschinger, C. Hempel, J. Home, F. Schmidt-Kaler, M. Biercuk, R. Blatt, S. Benjamin, and M. Müller, "Assessing the progress of trapped-ion processors towards fault-tolerant quantum computation," Phys. Rev. X **7**, 041061 (2017).
6. N. H. Nickerson, Y. Li, and S. C. Benjamin, "Topological quantum computing with a very noisy network and local error rates approaching one percent," Nat. Commun. **4**, 1756 (2013).

7. L. M. K. Vandersypen, M. Steffen, G. Breyta, C. S. Yannoni, M. H. Sherwood, and I. L. Chuang, "Experimental realization of Shor's quantum factoring algorithm using nuclear magnetic resonance," Nature **414**, 883–887 (2001).
8. B. Bartlett, A. Dutt, and S. Fan, "Deterministic photonic quantum computation in a synthetic time dimension," Optica **8**, 1515–1523 (2021).
9. J. L. Brien, "Optical quantum computing," Science **318**, 1567–1570 (2007).
10. J. L. O'Brien, G. J. Pryde, A. G. White, T. C. Ralph, and D. Branning, "Demonstration of an all-optical quantum controlled-NOT gate," Nature **426**, 264–267 (2003).
11. T. B. Pittman, M. J. Fitch, B. C. Jacobs, and J. D. Franson, "Experimental controlled-NOT logic gate for single photons in the coincidence basis," Phys. Rev. A **68**, 032316 (2003).
12. S. Gasparoni, J.-W. Pan, P. Walther, T. Rudolph, and A. Zeilinger, "Realization of a photonic controlled-NOT gate sufficient for quantum computation," Phys. Rev. Lett. **93**, 020504 (2004).
13. R. Okamoto, J. L. O'Brien, H. F. Hofmann, and S. Takeuchi, "Realization of a Knill-Laflamme-Milburn controlled-NOT photonic quantum circuit combining effective optical nonlinearities," Proc. Natl. Acad. Sci. USA **108**, 10067–10071 (2011).
14. Z. Zhao, A.-N. Zhang, Y.-A. Chen, H. Zhang, J.-F. Du, T. Yang, and J.-W. Pan, "Experimental demonstration of a nondestructive controlled-NOT quantum gate for two independent photon qubits," Phys. Rev. Lett. **94**, 030501 (2005).
15. J.-P. Li, X. Gu, J. Qin, D. Wu, X. You, H. Wang, C. Schneider, S. Höfling, Y.-H. Huo, C.-Y. Lu, N.-L. Liu, L. Li, and J.-W. Pan, "Heralded nondestructive quantum entangling gate with single-photon sources," Phys. Rev. Lett. **126**, 140501 (2021).
16. B. P. Lanyon, M. Barbieri, M. P. Almeida, T. Jennewein, T. C. Ralph, K. J. Resch, G. J. Pryde, J. L. O'Brien, A. Gilchrist, and A. G. White, "Simplifying quantum logic using higher-dimensional Hilbert spaces," Nat. Phys. **5**, 134–140 (2009).
17. H.-L. Huang, W.-S. Bao, T. Li, F.-G. Li, X.-Q. Fu, S. Zhang, H.-L. Zhang, and X. Wang, "Deterministic linear optical quantum Toffoli gate," Phys. Lett. A **381**, 2673–2676 (2017).
18. S. Ru, Y. Wang, M. An, F. Wang, P. Zhang, and F. Li, "Realization of a deterministic quantum Toffoli gate with a single photon," Phys. Rev. A **103**, 022606 (2021).
19. Q. Zeng, T. Li, X. Song, and X. Zhang, "Realization of optimized quantum controlled-logic gate based on the orbital angular momentum of light," Opt. Express **24**, 8186–8193 (2016).
20. R. B. Patel, J. Ho, F. Ferreyrol, T. C. Ralph, and G. J. Pryde, "A quantum Fredkin gate," Sci. Adv. **2**, e1501531 (2016).
21. T. Ono, R. Okamoto, M. Tanida, H. F. Hofmann, and S. Takeuchi, "Implementation of a quantum controlled-SWAP gate with photonic circuits," Sci. Rep. **7**, 45353 (2017).
22. A. Politi, M. J. Cryan, J. G. Rarity, S. Yu, and J. L. Brien, "Silica-on-silicon waveguide quantum circuits," Science **320**, 646–649 (2008).
23. G. D. Marshall, A. Politi, J. C. F. Matthews, P. Dekker, M. Ams, M. J. Withford, and J. L. O'Brien, "Laser written waveguide photonic quantum circuits," Opt. Express **17**, 12546–12554 (2009).
24. C. Anton, J. C. Loredo, G. Coppola, H. Ollivier, N. Viggianiello, A. Harouri, N. Somaschi, A. Crespi, I. Sagnes, A. Lemaitre, L. Lanco, R. Osellame, F. Sciarrino, and P. Senellart, "Interfacing scalable photonic platforms: solid-state based multi-photon interference in a reconfigurable glass chip," Optica **6**, 1471–1477 (2019).
25. S. Atzeni, A. S. Rab, G. Corrielli, E. Polino, M. Valeri, P. Mataloni, N. Spagnolo, A. Crespi, F. Sciarrino, and R. Osellame, "Integrated sources of entangled photons at the telecom wavelength in femtosecond-laser-written circuits," Optica **5**, 311–314 (2018).
26. Q. Zhang, M. Li, J. Xu, Z. Lin, H. Yu, M. Wang, Z. Fang, Y. Cheng, Q. Gong, and Y. Li, "Reconfigurable directional coupler in lithium niobate crystal fabricated by three-dimensional femtosecond laser focal field engineering," Photon. Res. **7**, 503–507 (2019).
27. F. Klauck, M. Heinrich, and A. Szameit, "Photonic two-particle quantum walks in Su–Schrieffer–Heeger lattices," Photon. Res. **9**, A1–A7 (2021).
28. A. Crespi, R. Ramponi, R. Osellame, L. Sansoni, I. Bongioanni, F. Sciarrino, G. Vallone, and P. Mataloni, "Integrated photonic quantum gates for polarization qubits," Nat. Commun. **2**, 566 (2011).
29. J. Zeuner, A. N. Sharma, M. Tillmann, R. Heilmann, M. Gräfe, A. Moqanaki, A. Szameit, and P. Walther, "Integrated-optics heralded controlled-NOT gate for polarization-encoded qubits," Npj Quantum Inf. **4**, 13 (2018).
30. N. Spagnolo, L. Aparo, C. Vitelli, A. Crespi, R. Ramponi, R. Osellame, P. Mataloni, and F. Sciarrino, "Quantum interferometry with three-dimensional geometry," Sci. Rep. **2**, 862 (2012).
31. A. Crespi, R. Osellame, R. Ramponi, M. Bentivegna, F. Flamini, N. Spagnolo, N. Viggianiello, L. Innocenti, P. Mataloni, and F. Sciarrino, "Suppression law of quantum states in a 3D photonic fast Fourier transform chip," Nat. Commun. **7**, 10469 (2016).
32. Z. Q. Jiao, J. Gao, W. H. Zhou, X. W. Wang, R. J. Ren, X. Y. Xu, L. F. Qiao, Y. Wang, and X. M. Jin, "Two-dimensional quantum walks of correlated photons," Optica **8**, 1129–1135 (2021).
33. H. Tang, C. Di Franco, Z.-Y. Shi, T.-S. He, Z. Feng, J. Gao, K. Sun, Z.-M. Li, Z.-Q. Jiao, T.-Y. Wang, M. S. Kim, and X.-M. Jin, "Experimental quantum fast hitting on hexagonal graphs," Nat. Photonics **12**, 754–758 (2018).
34. H. Tang, X.-F. Lin, Z. Feng, J.-Y. Chen, J. Gao, K. Sun, C.-Y. Wang, P.-C. Lai, X.-Y. Xu, Y. Wang, L.-F. Qiao, A.-L. Yang, and X.-M. Jin, "Experimental two-dimensional quantum walk on a photonic chip," Sci. Adv. **4**, eaat3174 (2018).
35. Q. Zhang, M. Li, Y. Chen, X. Ren, R. Osellame, Q. Gong, and Y. Li, "Femtosecond laser direct writing of an integrated path-encoded CNOT quantum gate," Opt. Mater. Express **9**, 2318–2326 (2019).
36. T. Meany, D. N. Biggerstaff, M. A. Broome, A. Fedrizzi, M. Delanty, M. J. Steel, A. Gilchrist, G. D. Marshall, A. G. White, and M. J. Withford, "Engineering integrated photonics for heralded quantum gates," Sci. Rep. **6**, 25126 (2016).
37. M. A. Nielsen and I. L. Chuang, *Quantum Computing and Quantum Information* (Cambridge University, 2000).
38. D. G. Cory, M. D. Price, W. Maas, E. Knill, R. Laflamme, W. H. Zurek, T. F. Havel, and S. S. Somaroo, "Experimental quantum error correction," Phys. Rev. Lett. **81**, 2152–2155 (1998).
39. A. Paetznick and B. W. Reichardt, "Universal fault-tolerant quantum computation with only transversal gates and error correction," Phys. Rev. Lett. **111**, 090505 (2013).
40. G. A. Barbosa, "Quantum half-adder," Phys. Rev. A **73**, 052321 (2006).
41. A. Odeh and E. Abdelfattah, "Quantum sort algorithm based on entanglement qubits {00, 11}," in *IEEE Long Island Systems, Applications and Technology Conference (LISAT)* (2016), pp. 1–5.
42. K. A. Brickman, P. C. Haljan, P. J. Lee, M. Acton, L. Deslauriers, and C. Monroe, "Implementation of Grover's quantum search algorithm in a scalable system," Phys. Rev. A **72**, 050306 (2005).
43. M. Mičuda, M. Miková, I. Straka, M. Sedlák, M. Dušek, M. Ježek, and J. Fiurášek, "Tomographic characterization of a linear optical quantum Toffoli gate," Phys. Rev. A **92**, 032312 (2015).
44. M. Mičuda, M. Sedlák, I. Straka, M. Miková, M. Dušek, M. Ježek, and J. Fiurášek, "Efficient experimental estimation of fidelity of linear optical quantum Toffoli gate," Phys. Rev. Lett. **111**, 160407 (2013).
45. Z. Liu, X. Yang, W. Han, R. Yan, T. Yan, and P. Wang, "Design of an optical Toffoli gate for reversible logic operation using silicon photonic integrated circuits," Proc. SPIE **11763**, 117633O (2021).
46. A. Barenco, C. H. Bennett, R. Cleve, D. P. DiVincenzo, N. Margolus, P. Shor, T. Sleator, J. A. Smolin, and H. Weinfurter, "Elementary gates for quantum computation," Phys. Rev. A **52**, 3457–3467 (1995).
47. E. Knill, R. Laflamme, and G. J. Milburn, "A scheme for efficient quantum computation with linear optics," Nature **409**, 46–52 (2001).
48. T. C. Ralph, K. J. Resch, and A. Gilchrist, "Efficient Toffoli gates using qudits," Phys. Rev. A **75**, 022313 (2007).
49. R. Heilmann, M. Gräfe, S. Nolte, and A. Szameit, "Arbitrary photonic wave plate operations on chip: realizing Hadamard, Pauli-X and rotation gates for polarisation qubits," Sci. Rep. **4**, 4118 (2014).
50. G. Corrielli, A. Crespi, R. Geremia, R. Ramponi, L. Sansoni, A. Santinelli, P. Mataloni, F. Sciarrino, and R. Osellame, "Rotated waveplates in integrated waveguide optics," Nat. Commun. **5**, 4249 (2014).

51. M. Li, Q. Zhang, Y. Chen, X. Ren, Q. Gong, and Y. Li, "Femtosecond laser direct writing of integrated photonic quantum chips for generating path-encoded Bell states," Micromachines **11**, 1111 (2020).
52. J. Wang, S. Paesani, Y. Ding, R. Santagati, P. Skrzypczyk, A. Salavrakos, J. Tura, R. Augusiak, L. Mančinska, D. Bacco, D. Bonneau, J. W. Silverstone, Q. Gong, A. Acín, K. Rottwitt, L. K. Oxenløwe, J. L. O'Brien, A. Laing, and M. G. Thompson, "Multidimensional quantum entanglement with large-scale integrated optics," Science **360**, 285–291 (2018).
53. T. B. Pittman, B. C. Jacobs, and J. D. Franson, "Probabilistic quantum logic operations using polarizing beam splitters," Phys. Rev. A **64**, 062311 (2001).
54. J. Fiurášek, "Linear-optics quantum Toffoli and Fredkin gates," Phys. Rev. A **73**, 062313 (2006).
55. C. K. Hong, Z. Y. Ou, and L. Mandel, "Measurement of subpicosecond time intervals between two photons by interference," Phys. Rev. Lett. **59**, 2044–2046 (1987).
56. B. J. Metcalf, J. B. Spring, P. C. Humphreys, N. Thomas-Peter, M. Barbieri, W. S. Kolthammer, X.-M. Jin, N. K. Langford, D. Kundys, J. C. Gates, B. J. Smith, P. G. R. Smith, and I. A. Walmsley, "Quantum teleportation on a photonic chip," Nat. Photonics **8**, 770–774 (2014).
57. X.-M. Xiu, X. Geng, S.-L. Wang, C. Cui, Q.-Y. Li, Y.-Q. Ji, and L. Dong, "Construction of a polarization multiphoton controlled one-photon unitary gate assisted by the spatial and temporal degrees of freedom," Adv. Quantum Technol. **2**, 1900066 (2019).
58. L. Dong, S.-L. Wang, C. Cui, X. Geng, Q.-Y. Li, H.-K. Dong, X.-M. Xiu, and Y.-J. Gao, "Polarization Toffoli gate assisted by multiple degrees of freedom," Opt. Lett. **43**, 4635–4638 (2018).